buildings

Article

Analysis of Natural Vibration Characteristics of Metal Roof Panel of Large-Span Standing-Seam Metal Roof System

Zhen Xie [1,2] and Yongshan Zhang [2,*]

[1] Hunan Industrial Equipment Installation Co., Ltd., Changsha 412000, China; 2112016244@e.gzhu.edu.cn
[2] School of Civil Engineering, Guangzhou University, Guangzhou 510006, China
* Correspondence: gzewdsx@163.com

Abstract: Metal roof systems are widely used in various landmark buildings. Understanding the natural vibration characteristics and primary influence of the roof system is useful for improving the roof system's service life and maintaining the project's safety. In addition, it is helpful to analyze the vibration force of the structure under earthquake and wind load. In this paper, the experimental investigation of the natural vibration characteristics (NVC) of two commonly used structural forms of standing-seam metal roof systems is carried out, and the influence of different boundary conditions, specimen width, panel width, and other parameters on the NVC are considered. The influence of different factors on the NVC of the roof system is analyzed in detail, and the main influencing factors and secondary influencing factors are studied. The research results show apparent differences in the NVC of the side and middle span of the roof panel under different parameters. The structural form has the most significant influence on the NVC of the roof panel, and the maximum influence on the peak acceleration (PA) and the fundamental frequency (FF) of the roof panel are 83.7% and 60%, respectively. The width of the specimen has a minor influence on the FF of the roof panel, and the minimum influence range is 6.9%. The influence of structural form, constraint form, specimen width, and panel width on the PA of the roof panel is far more significant than it is on the FF, with the difference between the two reaching 44.2%.

Keywords: metal roof system; large span; roof panel; natural vibration characteristic; experimental investigation; parametric analysis

Citation: Xie, Z.; Zhang, Y. Analysis of Natural Vibration Characteristics of Metal Roof Panel of Large-Span Standing-Seam Metal Roof System. *Buildings* **2023**, *13*, 2855. https://doi.org/10.3390/buildings13112855

Academic Editor: Carmelo Gentile

Received: 23 September 2023
Revised: 2 November 2023
Accepted: 9 November 2023
Published: 14 November 2023

1. Introduction

The mature application of cold bending forming technology brings excellent development opportunities for applying thin metal roof panels in building envelopes, and the metal roof system has been increasingly widely used [1,2]. In terms of materials, from the initial galvanized steel sheet, it has developed into aluminized zinc steel sheet, titanium zinc sheet, aluminum alloy sheet, copper sheet, and stainless steel sheet. From the perspective of structural form, from the initial form of self-tapping screw penetration, it has developed into a safer, more attractive and practical new structural form in areas such as occlusion, curling, locking, and welding. In terms of application scope, it has been widely used everywhere from civil public buildings to industrial factory buildings [3]. With the increase of practical application cases, more and more problems of metal roofs are gradually exposed, including insufficient wind resistance, roof leakage, and durability [4]. The natural frequency and modal analysis of the structure are carried out, which increases understanding of the dynamic characteristics of the structure. The research results showed that the structure's resonance can cause significant harm to the structure [5]. As a typical large-span structure, it is of great significance for engineering design and application to understand the natural vibration characteristic of metal roof systems and reduce the resonance phenomenon between the structure and the external environment.

The existing research on metal roof systems mainly focuses on wind resistance. Sivapathasundaram carried out experimental and numerical simulation studies on standing-seam aluminum alloy roof systems. The failure curves of purlins were established to determine the damage degree of roof panels under extreme wind loads, and feasible reinforcement measures were proposed [6,7]. Morrison simulated the standing-seam metal roof with wind clips and solved its wind-resistance capacity [8]. The validity of the numerical simulation method is verified by comparing the experimental results. Kumar [9] proposed a method for assessing wind-induced fatigue damage using Miner's rule and Goodman's method. The rain flow technique was used to analyze the wind pressure data, and the probability method was used to evaluate the fatigue characteristics of the long-term wind climate and pressure in the region. Myuran carried out a dynamic fatigue loading test on the mechanical properties of the standing-seam roof system. A calculation method for the fatigue performance of the roof system is proposed [10,11]. Schroter measured the wind-resistance capacity of a specific plate type by static pressure test [12]. In addition, Ali replaces the contact between the standing-seam roof panels with contact elements, obtains the metal roof's vibration mode and natural frequency through modal analysis, and further determines the dynamic characteristics of the roof system under dynamic loads [13]. Li [14] carried out a modal analysis on the roof panel of a continuous welded stainless steel roof system using a test and finite element. The research shows that the fundamental frequency of roof panels is 16.72 Hz.

Many scholars have conducted studies on the natural vibration characteristic of large-span structures. The structure's natural frequency is one of the important indexes to measure the dynamic characteristics, which will provide an essential theoretical basis for the wind resistance, seismic design, and structural health monitoring of the box girder bridge [15]. The analysis methods of natural vibration characteristics of box girder bridges include the energy variational method, matrix analysis method, finite element method, and test method. Among them, the energy variational method is the most commonly used analytical method to study the natural vibration frequency of box girder bridges [16–18]. Zhang et al. derived the variational solution of the bending natural vibration characteristics of composite box girder bridges with corrugated steel webs considering the influence of shear lag and the accordion effect. They revealed two kinds of results [19]. Based on Hamilton's principle, Jiang et al. established an analytical method for the bending natural frequency of box girders considering the effects of shear deformation, shear lag, and moment of inertia [20]. Based on higher-order theory and the Carrera closed-form solution, Shen et al. analyzed the free vibration characteristics of steel–concrete composite beams [21]. In addition, Liu et al. conducted theoretical analysis on the vibration characteristics of fiber metal laminates thin plates under cantilever boundary conditions and compared the experimental results to verify the reliability of the calculation model [22]. In addition, many scholars have conducted a series of theoretical and numerical analysis studies on the bending and vibration characteristics of thin plate and beam members [23–27]. The above research is mainly based on the background of nonlocal continuum theory, and considers the free vibration and forced vibration of plates from macro to nano. The modal-based method is used to analyze the vibration of the above structure. These methods are more advanced than the commonly used elastic theory used to analyze the macro structure. This paper can refer to the relevant research methods and conclusions to carry out the dynamic characteristics analysis of the metal roof system.

In summary, the study on the metal roof system considered its wind resistance performance and rarely analyzes the natural frequency and modal distribution of the metal roof system itself. The research on the NVC of large-span structures, thin plate and beam members is mainly focused on long-span bridges, and there is little analysis of the natural vibration frequency and modal analysis of large-span metal roof systems. This paper refers to the research methods and ideas of the NVC of large-span bridge structures. It conducts experimental research on the NVC of the standing-seam metal roof system. The effects of different roof system structure forms, sizes, occlusion forms, and boundary conditions on the dynamic characteristics of the standing-seam roof system are considered. The influence of different parameters on the NVC of the roof system is compared and analyzed, and the primary factors and secondary factors are understood. The research results of this paper can provide some reference for other types of metal roof systems and provide critical data support for engineering design and application.

2. Experimental Program

2.1. Test Specimens

In this paper, the experimental study of the natural vibration frequency of four test specimens is carried out. The four roof systems consider different parameters, and the parameters' influence on the roof system's NVC is compared and analyzed. The four specimens are all standing-seam metal roof systems. The plane and section diagrams of the specimens are shown in Figure 1. The length of all specimens was 7500 mm. In specimen A, the width of the roof system and a single roof panel are 2000 mm and 420 mm, respectively. The roof system is 360° occlusion form, and the roof panel used 0.8 mm thick aluminized zinc profiled steel sheet. The purlin is a square steel tube with a cross-section length of 150 mm and a width of 100 mm. Figure 1a shows specimen A's plane and section diagrams. In specimen B, the width of the roof system and a single roof panel are 3660 mm and 420 mm, respectively. The occlusion and structural form of specimen B is the same as that of specimen A, and the plane diagram of specimen B is illustrated in Figure 1b. In specimen C, the width of the roof system is 3860 mm, and the width and thickness of a single roof panel are 300 mm and 1.0 mm, respectively. The roof panel is made of aluminum–magnesium–manganese material, and specimen C is 270° occlusion form. The plane and section diagrams of specimen C are plotted in Figure 1c. In specimen D, the width of the roof system is 3660 mm, and the width and thickness of a single roof panel are 400 mm and 1.0 mm, respectively. The occlusion and structural form of specimen D is the same as that of specimen C, and the plane diagram of specimen D is drawn in Figure 1d.

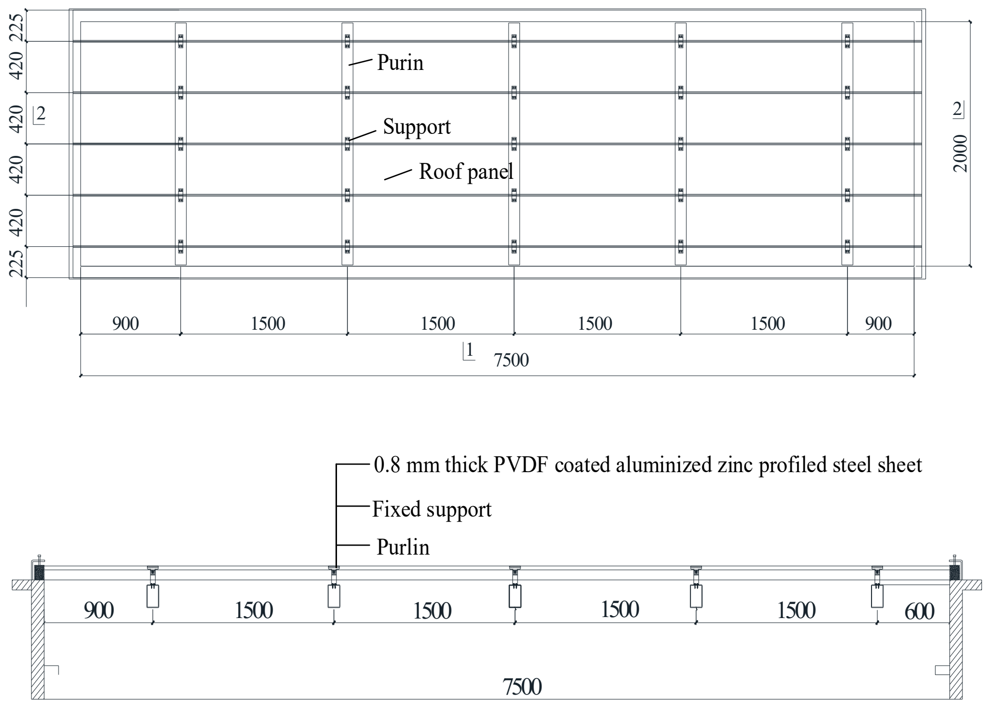

(**a**) Specimen A

Figure 1. *Cont.*

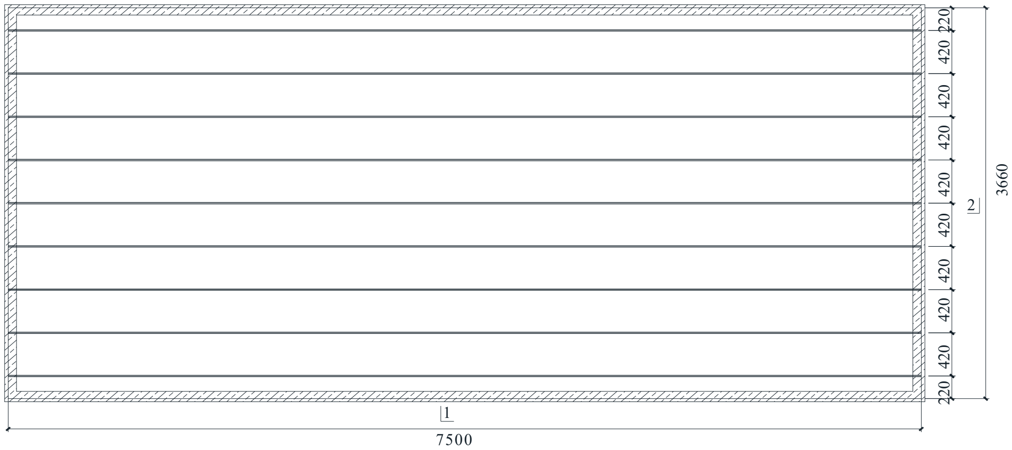

(**b**) Specimen B

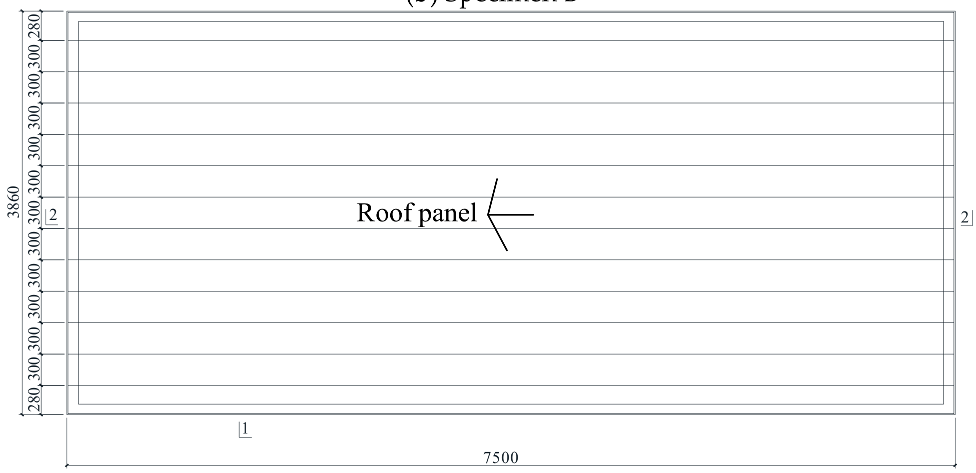

Plane diagram

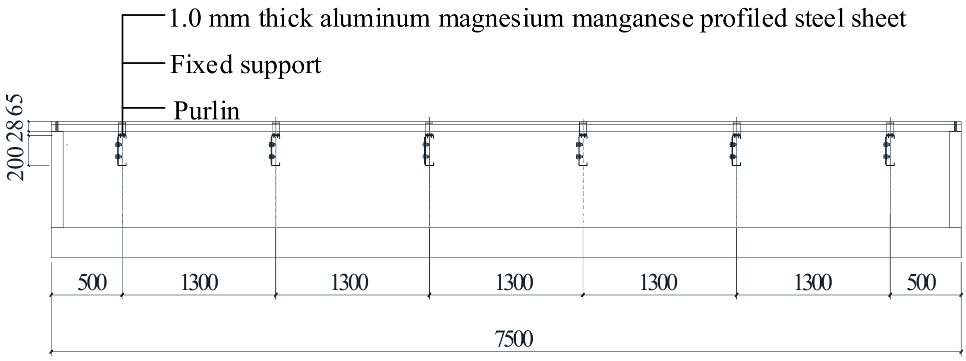

Section diagram

(**c**) Specimen C

Figure 1. *Cont.*

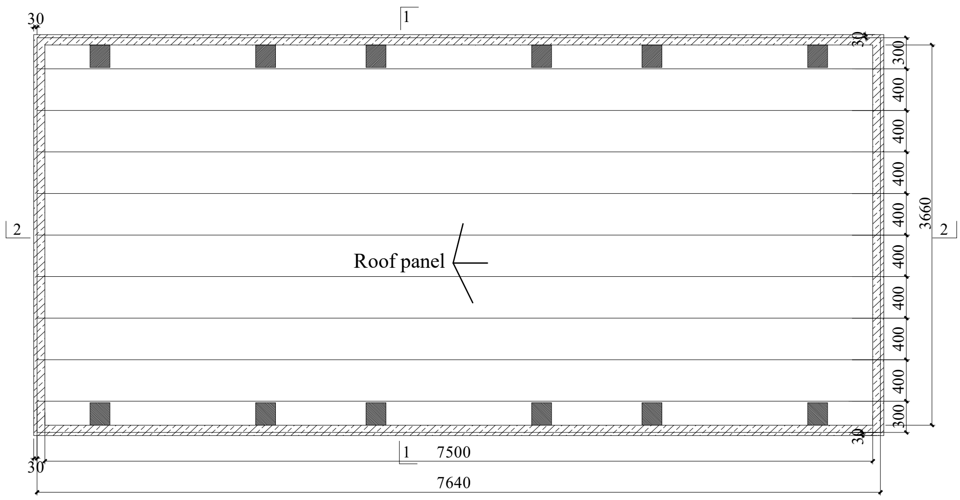

(**d**) Specimen D

Figure 1. Diagram of specimens.

2.2. Sensor Arrangement

In this paper, the natural frequency of the four specimens is tested by the uTekL8916 dynamic signal analysis system and 941B ultra-low frequency vibrometer. In the four specimens, the sensors are selected at different positions of the roof panel's side and middle span to analyze the NVC. Six sensors are arranged for each specimen, as shown in Figure 2. The sensors of A1~A6 are arranged on specimen A, among which A1~A3 are arranged at the roof panel of the side span purlin position, and A4~A6 are arranged at the non-purlin roof panel of the middle span. The sensors of B1~B6 are arranged on specimen B, where B1~B3 are set in the side span, and B4~B6 are set in the middle span. The sensors of C1~C6 are installed on specimen C, where C1~C3 is on the side span, and C4~C6 is on the middle span. The sensors of D1~D6 are installed on specimen D, in which D1~D3 are arranged in the side span, and D4~D6 are laid in the middle span. The difference between the natural frequency of the side span and the middle span roof panel and the frequency variation law at different positions along the length direction of the roof panel are compared and analyzed.

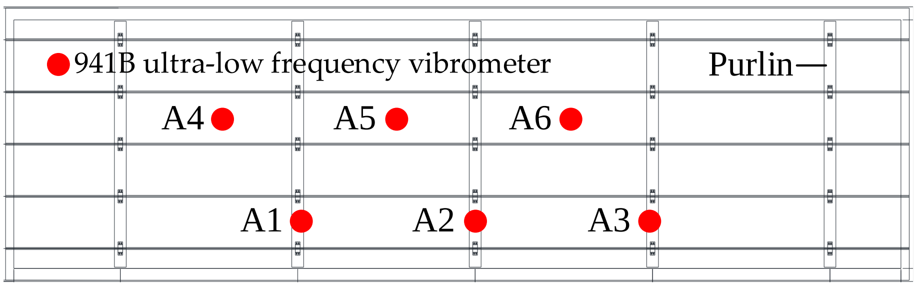

（a）Specimen A

Figure 2. *Cont.*

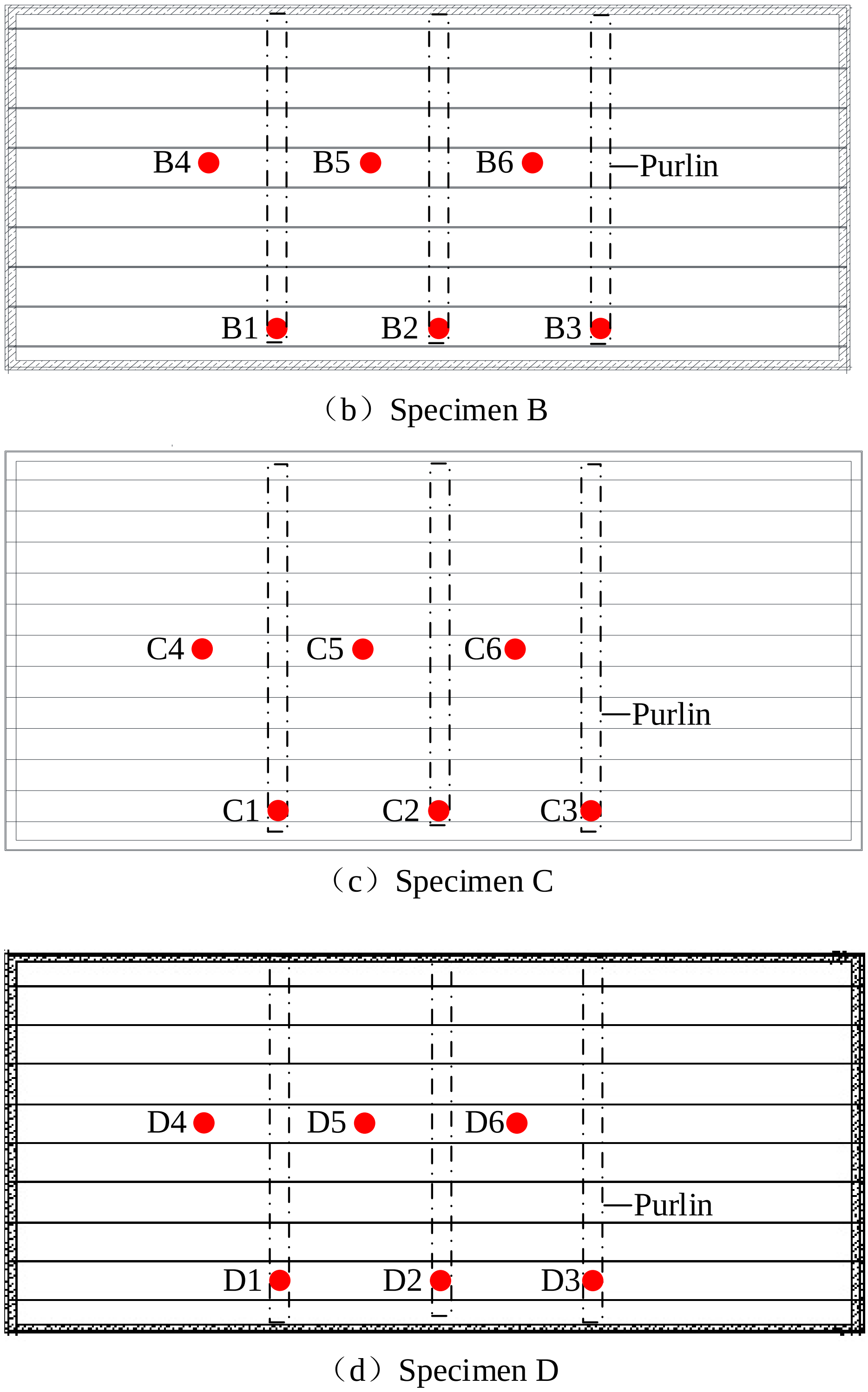

Figure 2. Sensors arrangement of the understudied specimens.

2.3. Test Scheme

As seen above, this paper arranges three sensors in the specimen's side and middle span, respectively, and analyzes the natural vibration frequency at different spans of the test specimens. To further analyze the influence law of the dynamic behavior of the test specimens, the influence of different boundary constraint forms on the natural vibration frequency of the roof panel is considered. Further, the relationship between the natural frequency of the roof panel and the external environmental load frequency can be analyzed, and whether the two will produce a resonance phenomenon can be judged. This paper shows the specific cases and parameters of the four specimens in Table 1. Specimen A considers three types of boundary constraints, namely, four-sided free (4SF), four-sided constraint (4SC), and two-sided constraint (2SC). Specimen B only is considered the form of four-sided constraint (4SC). Specimen C applies three types of constraints, namely, two-sided constraint (2SC), three-sided constraint (3SC), and four-sided constraint (4SC). Specimen D is applied in the form of four-sided constraint (4SC). In cases S1~S3 and S5~S6, the influence of different constraints on the NVC of aluminum–zinc alloy (AZA) and aluminum–magnesium–manganese (AMM) roof panels are studied. In cases S3 and S4, the influence of different specimen widths on the natural frequency of the roof panel is researched. The specimen widths of cases S3 and S4 are 2000 mm and 3660 mm, respectively. Cases S7 and S8 are considered the influence of roof panel width on the dynamic behavior of the roof system. The roof system widths of cases S7 and S8 are 2000 mm and 3660 mm, respectively. The boundary of the roof system is constrained and fixed by steel angle codes and bolts, and the constraint test diagram is shown in Figure 3. In addition, the influence of different roof system structure forms on the dynamic property is compared. In this paper, the hammering method is used to measure the natural vibration characteristics of the roof system. Each case is hammered three times, and the average value of the three results is selected for analysis. The specimen is basically in an elastic state, without considering the wear of the component. The acquisition equipment mainly includes the uTekL8916 dynamic signal analysis system and 941B ultra-low frequency vibrometer. The dynamic load is applied to the specimen by the rubber hammer, and the comprehensive results are obtained by setting different sensors on the roof panel. Then, the roof panel's PA and FF are analyzed.

Table 1. The specific parameters and test cases of the specimen.

Cases	Specimen	Panel Material	Panel Width (mm)	Occlusion Form (°)	Boundary Conditions
S1	A	AZA	420	360	4SF
S2	A	AZA	420	360	4SC
S3	A	AZA	420	360	2SC
S4	B	AZA	420	360	4SC
S5	C	AMM	300	270	2SC
S6	C	AMM	300	270	3SC
S7	C	AMM	300	270	4SC
S8	D	AMM	400	270	4SC

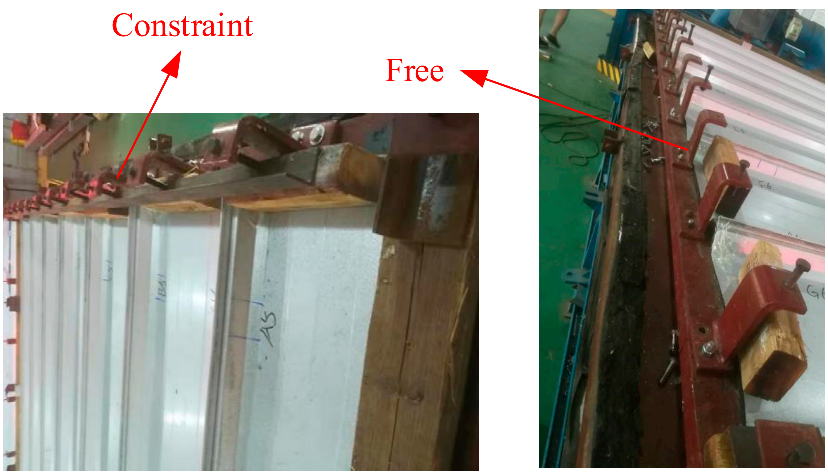

Figure 3. Boundary constraint form of the roof system.

3. Analysis of Test Results

3.1. Case S1

The acceleration time–history curve of case S1 is illustrated in Figure 4. The acceleration change rules of the side span and middle span are similar. The PA of sensors A1~A6 is shown in Figure 5. The PA of A1~A6 were 4.24 m/s^2, 4.48 m/s^2, 4.46 m/s^2, 3.17 m/s^2, 4.16 m/s^2, 4.13 m/s^2, respectively. The PA of the side span roof panel is greater than that of the middle span, and the maximum difference is 25.2%. Along the length direction of the roof panel, the PA of the side span and the middle span show an increasing trend, and the maximum decline was 5.2% and 31.2%, respectively.

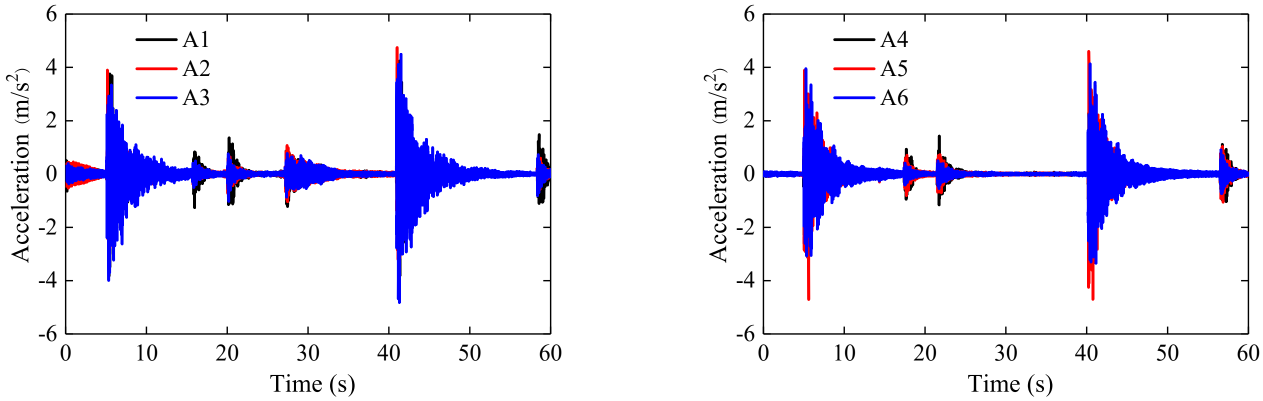

(**a**) Side span (**b**) Mid-span

Figure 4. Acceleration time-history plot of case S1.

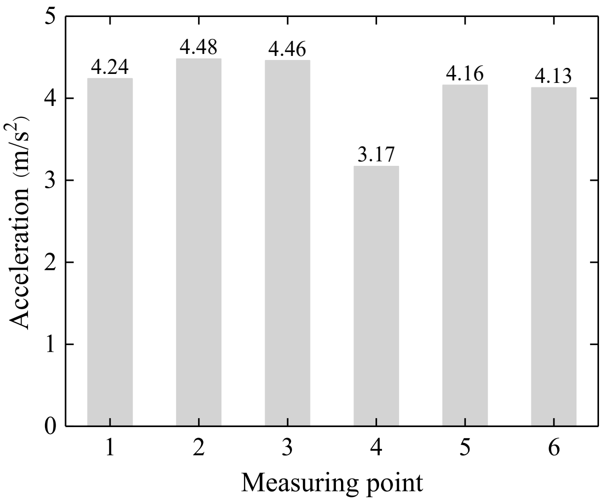

Figure 5. The PA of case S1.

The frequency and acceleration curves of S1 are drawn in Figure 6. It can be found that the frequencies of sensors A1~A6 under the FF are 15.00 Hz, 15.00 Hz, 13.50 Hz, 15.00 Hz, 15.00 Hz, and 13.50 Hz, respectively. The frequency difference between the side and middle span under the FF is insignificant. The primary frequencies of the side and middle span appear at 13.50 Hz and 33 Hz, respectively. The natural frequency of the S1 roof panel is about 15 Hz. Compared with the reference results [14], the maximum error is about 10.2%. As can be found, the test results of this paper have a certain accuracy.

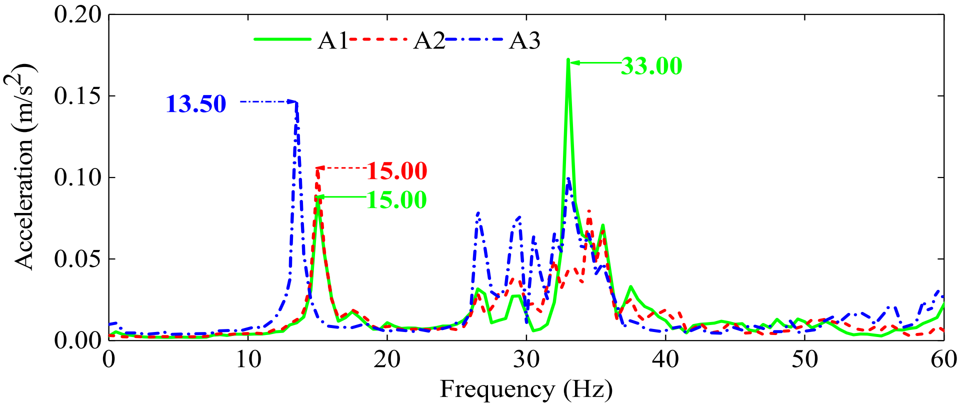

(**a**) Side span.

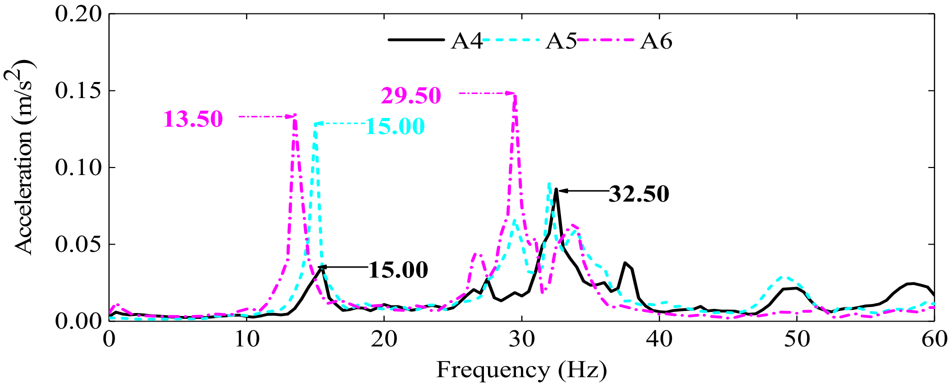

(**b**) Mid-span

Figure 6. Frequency and acceleration curve of case S1.

To further analyze the dynamic characteristics of the roof panel, the damping ratio of the roof panel is calculated. The general methods for solving the damping ratio mainly include the half-power bandwidth and time-domain attenuation methods [28,29]. In this paper, the half-power bandwidth method is used to calculate the damping ratio of the roof panel. Taking the working condition S1 as an example, the damping ratio is calculated for the measuring points A1~A6, and then the average value is taken. The fundamental frequencies of measuring points A1~A6 are given in Figure 6. Two frequencies corresponding to the fundamental frequency of 0.707 are selected and calculated according to Formula (1). The damping ratio of the roof panel is calculated to be 0.02.

$$\xi = \frac{f2 - f1}{f2 + f1} \tag{1}$$

3.2. Different Boundary Conditions

(1) Specimen A

Specimen A's acceleration time–history curves under different constraint forms are similar, as shown in Figure 7. With the change of the constraint form, the variation of acceleration in cases S1~S3 is different. The PA of each sensor under three cases is plotted in Table 2. The acceleration peaks of S1~S3 were 4.48 m/s^2, 4.81 m/s^2 and 3.84 m/s^2, respectively. The PA of S2 is significantly greater than that of S1 and S3. The variation of the PA of each sensor is illustrated in Figure 8. With the change in the constraint form, the variation law of the PA of the sensor is quite different. In the side span, the PA of A2 in case S2 (4FC) has a sudden change. The maximum difference in PA of the three cases is 47.4%. In the middle span, the PA of the sensor A5 in case S2 changes suddenly. The maximum difference in PA of the three cases is 29.3%. The PA of sensor A4 is the smallest under three cases. With the change of the constraint form, the influence on the acceleration of the side span is greater than that of the middle span.

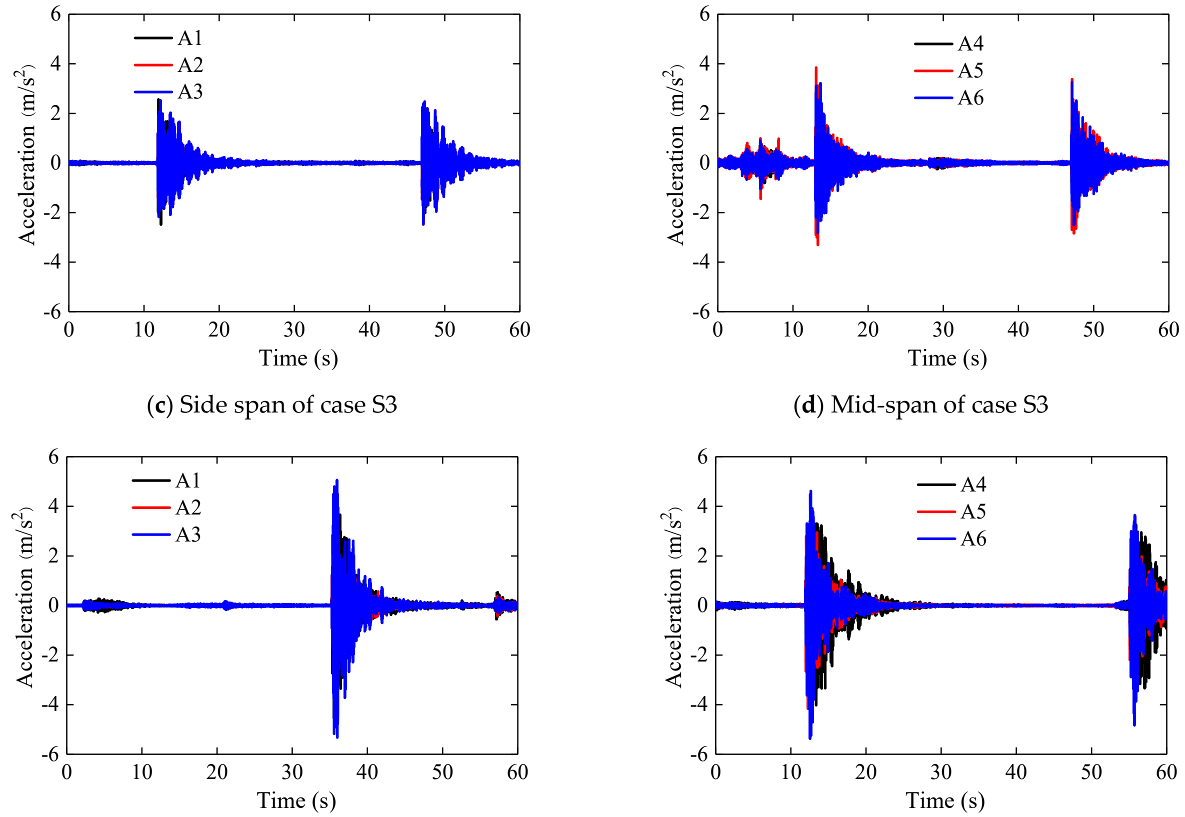

(**c**) Side span of case S3 (**d**) Mid-span of case S3

(**a**) Side span of case S2 (**b**) Mid-span of case S2

Figure 7. Acceleration time-history plot of cases S2 and S3.

Table 2. The PA of cases S1~S3 (m/s^2).

Cases	Specimen	Constraint Forms	1	2	3	4	5	6
S1	A	4SF	4.24	4.48	4.46	3.17	4.16	4.13
S2	A	4SC	3.43	2.35	4.81	3.39	2.94	4.48
S3	A	2SC	2.56	2.52	2.53	2.26	3.84	3.22

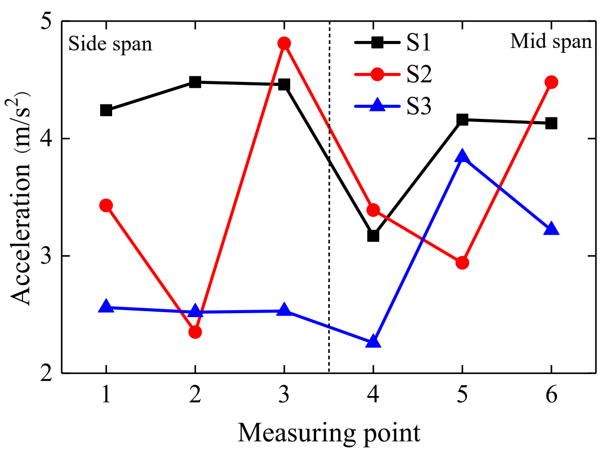

Figure 8. The variation curve of PA of cases S1~S3.

To further analyze the NVC of specimen A, the frequency spectrum curves of cases S2 and S3 are shown in Figure 9. With the change of the constraint form, the PA of the spectrum curve of specimen A is different. The natural frequency of the first order of the roof panel is analyzed. The natural frequency of the first order under three cases is listed in Table 3. In the side span, the maximum values of the first-order natural frequencies of the cases S1~S3 are the same, and the minimum values are 13.5 Hz, 14.4 Hz, and 14 Hz, respectively. With the change of constraint form, the minimum value of the natural frequency of the first order increases, and the maximum increase is 6.7%. In the middle span, the maximum value of the natural frequency of the first order of the cases S1~S3 appears in case S1, and the minimum values are 13.5 Hz, 14.5 Hz, and 13.7 Hz, respectively. With the change of the constraint form, the minimum value of the FF increases by 7.4%. It can be seen that the change of the constraint form has little effect on the natural frequency of the side span and the middle span roof panel.

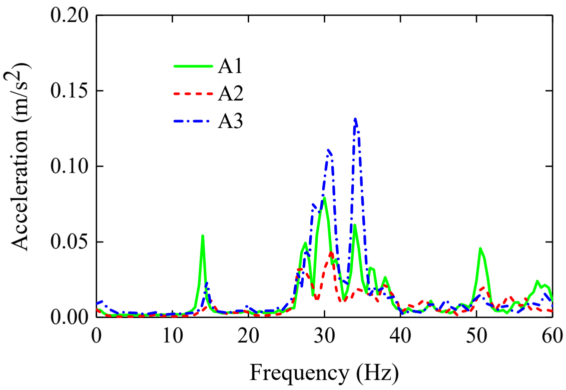

(**a**) Side span of case S2

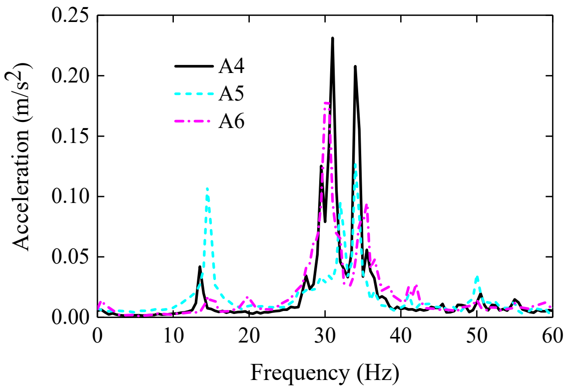

(**b**) Mid-span of case S2

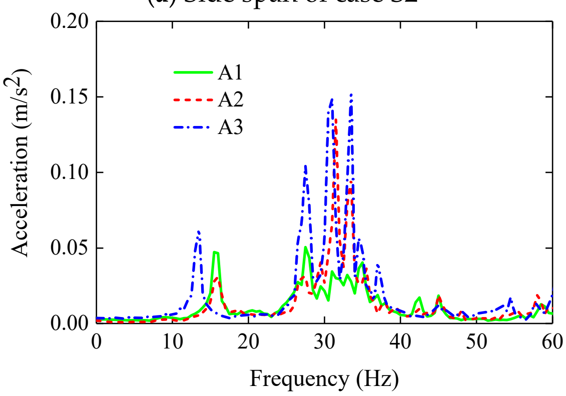

(**c**) Side span of case S3

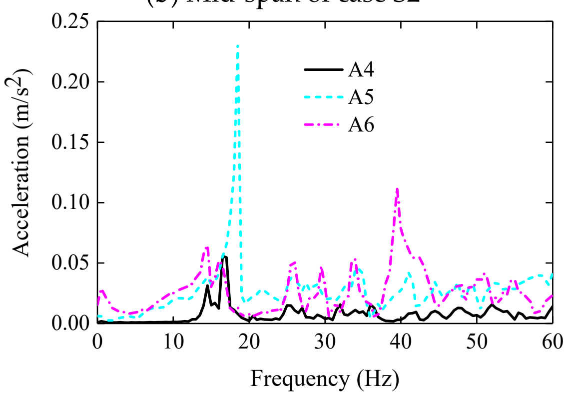

(**d**) Mid-span of case S3

Figure 9. Frequency and acceleration curve of cases S2 and S3.

Table 3. The FF of cases S1~S3 (Hz).

Cases	Specimen	Constraint Forms	1	2	3	4	5	6
S1	A	4SF	15.0	15.0	13.5	15.0	15.0	13.5
S2	A	4SC	14.4	14.5	15.0	14.5	14.5	14.5
S3	A	2SC	15.0	15.0	14.0	13.7	14.5	14.5

(2) Specimen C

The acceleration time–history curve of each sensor under different constraint forms (Specimen C) is shown in Figure 10. With the change of constraint form, the PA of each sensor is different. The PA of each sensor under different cases is plotted in Table 4. In the side span, the acceleration at the sensor C1 is the largest, and the acceleration of the sensor C6 is the smallest. With the change of constraint form, the acceleration of each sensor shows a downward trend. The maximum decrease of sensors C1~C3 was 25%, 7.8%, and 43.5%, respectively. In the middle span, the acceleration at the sensor C5 is the largest, and the acceleration at the sensor C6 is the smallest. With the change of constraint form, the acceleration of each sensor shows a downward trend. The maximum decrease of sensors C4~C6 was 25.2%, 26%, and 3.3%, respectively. It can be seen that the maximum influence of the change of the constraint form on the PA of the side span and the middle span of the specimen C is 43.5% and 26%, respectively.

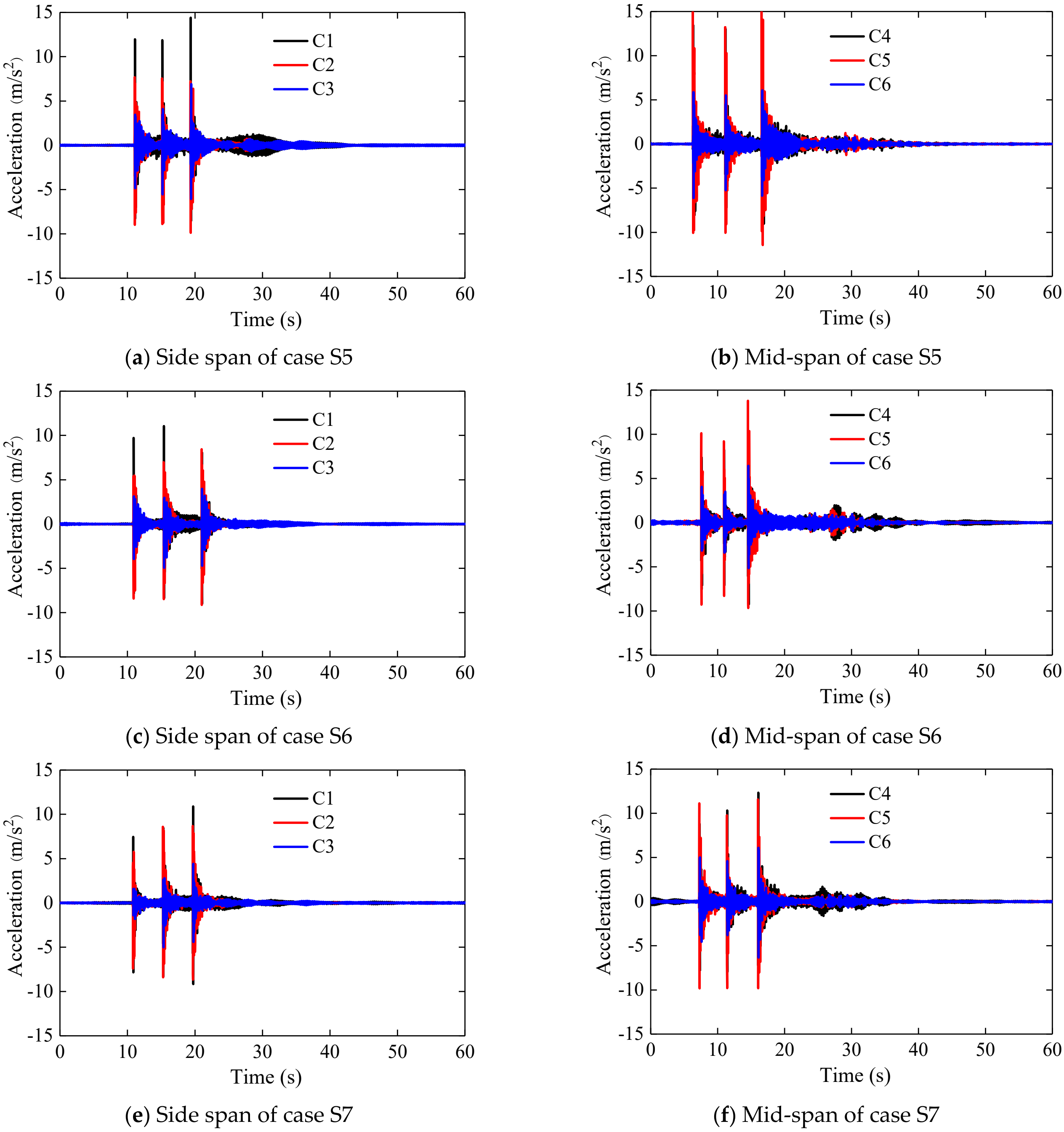

Figure 10. Acceleration time-history plot of cases S5~S7.

Table 4. The PA of cases S5~S7 (m/s^2).

Cases	Specimen	Constraint Forms	1	2	3	4	5	6
S5	C	2SC	14.4	7.7	6.9	13.9	15	6.1
S6	C	3SC	11.0	7.5	3.9	10.4	13.8	5.9
S7	C	4SC	10.8	7.1	4.4	12.3	11.1	6.0

To analyze the influence of constraint form on the natural frequency of specimen C, the frequency spectrum curves under different working conditions are shown in Figure 11. Under different constraint forms, the FF of each sensor is listed in Table 5. With the change in the constraint form, the FF of the sensor shows a downward trend. The maximum decrease of sensors C1~C6 are 14.3%, 14.3%, 20%, 17.1%, 19.4% and 17.1%, respectively. It can be found that the maximum influence of the constraint form on the FF of specimen C is about 20%.

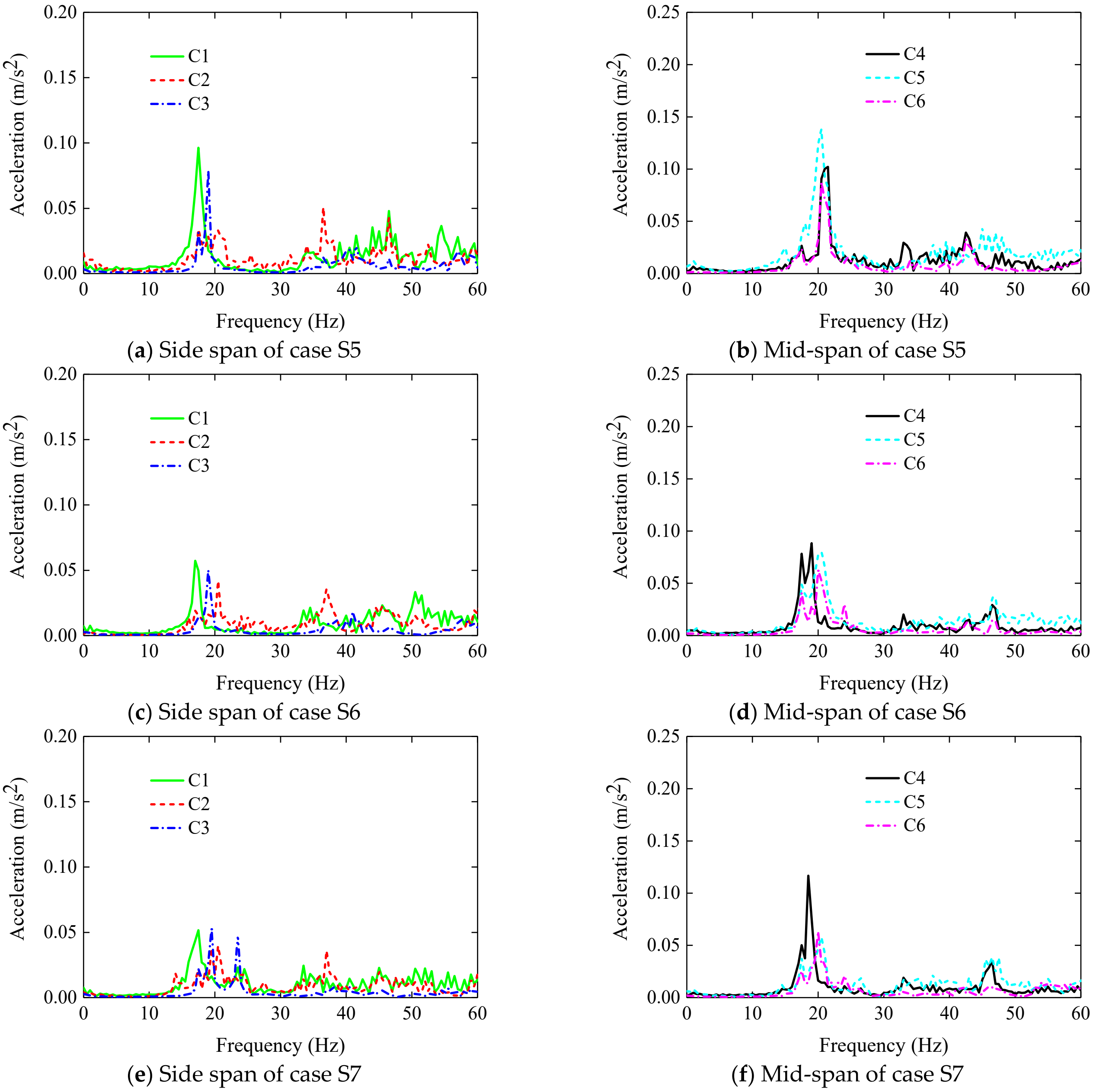

(**a**) Side span of case S5 (**b**) Mid-span of case S5
(**c**) Side span of case S6 (**d**) Mid-span of case S6
(**e**) Side span of case S7 (**f**) Mid-span of case S7

Figure 11. Frequency and acceleration curve of cases S5~S7.

Table 5. The FF of cases S5~S7 (Hz).

Cases	Specimen	Constraint Forms	1	2	3	4	5	6
S5	C	2SC	17.5	17.5	17.5	17.5	18.0	17.5
S6	C	3SC	17.0	17.0	17.5	17.5	17.5	17.5
S7	C	4SC	15.0	15.0	14.0	14.5	14.5	14.5

3.3. Different Specimen Width

Cases S2 and S4 are considered with different specimen widths, and the acceleration time–history curve of S4 is shown in Figure 12. The acceleration peaks of cases S2 and S4 are plotted in Table 6. In the side span, the PA of case S4 is greater than that of S2. The PA of cases S2 and S4 are 4.8 m/s^2 and 5.0 m/s^2, respectively. The maximum difference between the sensors is 50%, appearing at the sensor 2 position. In the middle span, the PA of case S4 is less than that of S2. The PA of cases S2 and S4 are 4.5 m/s^2 and 2.3 m/s^2, respectively. The maximum difference between the sensors is 51.1%. The comparative analysis shows that the specimen's width significantly influences the PA of the roof panel, and the maximum influence amplitude is 51.1%, appearing at the sensor 6 position.

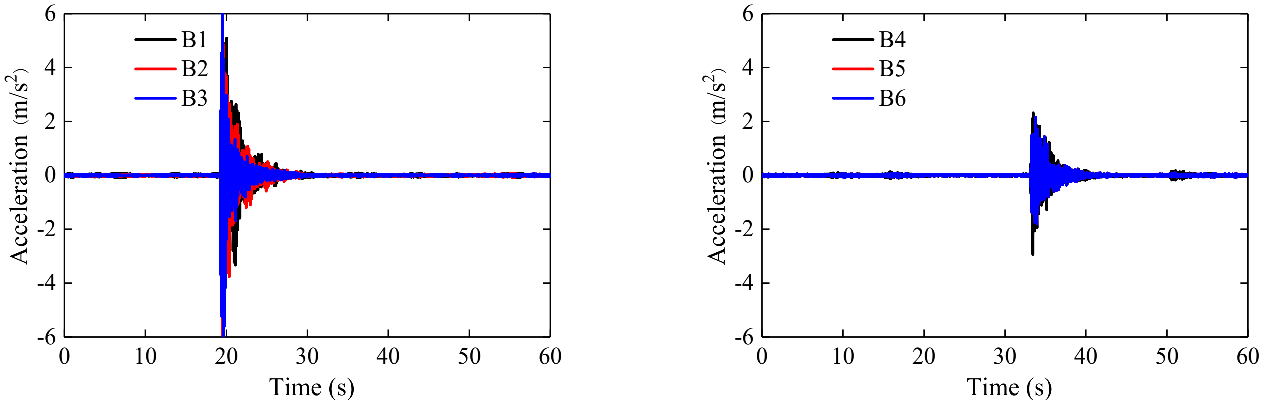

(**a**) Side span (**b**) Mid-span

Figure 12. Acceleration time-history plot of case S4.

Table 6. The PA of cases S2 and S4 (m/s^2).

Cases	Specimen	Constraint Forms	1	2	3	4	5	6
S2	A	4SC	3.4	2.4	4.8	3.4	2.9	4.5
S4	B	4SC	5.0	4.8	5.1	2.3	2.2	2.2

The spectrum curve of case S4 is shown in Figure 13. The first-order natural frequencies of cases S2 and S4 are drawn in Table 7. It can be seen that with the change in the width of the specimen, the changing trend of the FF of the roof panel is similar. The FF of specimens A and B at each roof panel position remains unchanged. The width of the specimen has little effect on the first natural frequency of the roof panel, and the maximum influence amplitude is about 6.9%.

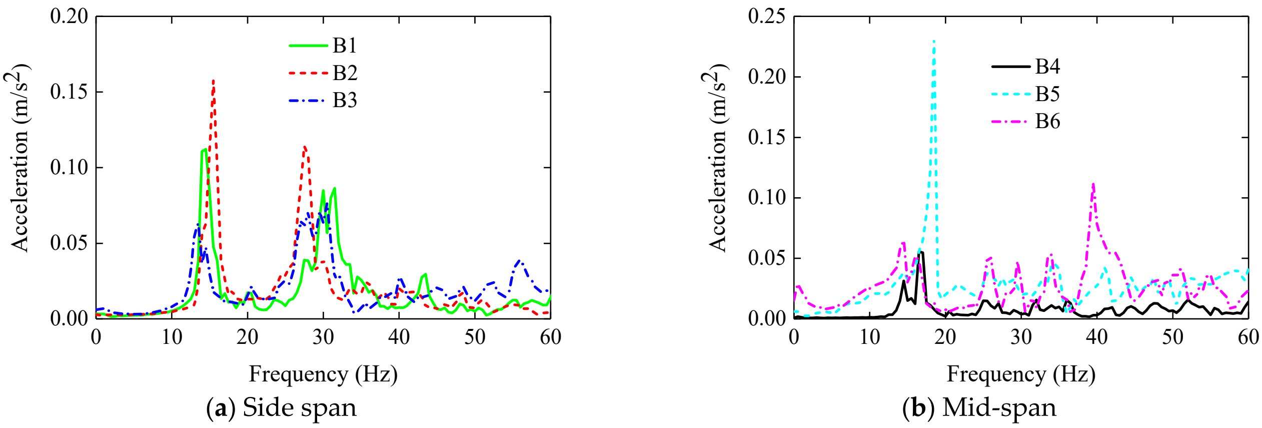

Figure 13. Frequency and acceleration curve of case S4.

Table 7. The FF of cases S2 and S4 (Hz).

Cases	Specimen	Constraint Forms	1	2	3	4	5	6
S2	A	4SC	14.4	14.5	15	14.5	14.5	14.5
S4	B	4SC	14.5	15.5	14.5	14.5	14.5	14.5

3.4. Different Panel Width

The cases S7 and S8 are considered with different panel widths and the acceleration time–history curve of S8 is plotted in Figure 14. The acceleration peaks of cases S7 and S8 are illustrated in Table 8. The PA of case S8 is greater than that of case S7. In the two cases, the acceleration at the position of sensor 3 is the smallest. The PA of case S7 appears in the side span sensor 4, and the PA of case S8 appears in the middle span sensor 2. The PA of cases S7 and S8 are 12.3 m/s^2 and 15.0 m/s^2, respectively. The maximum difference in PA of cases S7 and S8 in the side and middle span is 52.6% and 54.2%, respectively.

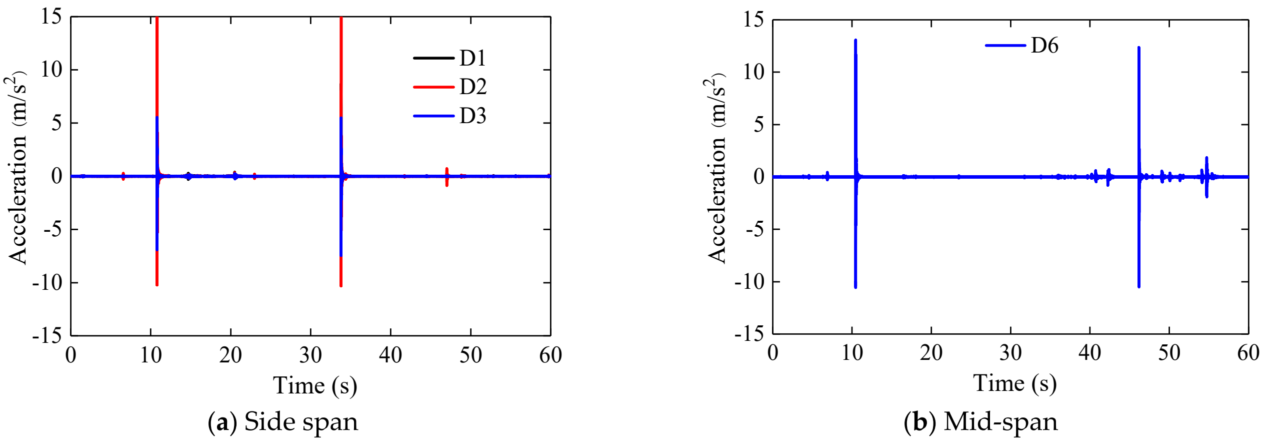

Figure 14. Acceleration time-history plot of case S8.

Table 8. The PA of cases S7 and S8 (m/s^2).

Cases	Specimen	Constraint Forms	1	2	3	4	5	6
S7	C	4SC	10.8	7.1	4.4	12.3	11.1	6.0
S8	D	4SC	9.0	15.0	5.5	10.6	13.5	13.1

The spectrum curve of case S8 is shown in Figure 15. The first-order natural frequencies of cases S7 and S8 are drawn in Table 9. It can be found that the FF of case S7 is significantly larger than that of case S8. The FF of the two cases at different roof panel positions remains unchanged. The maximum FF of cases S7 and S8 are 15.0 Hz and 9.0 Hz, respectively. The maximum difference between the side and middle spans is 40% and 37.9%, respectively.

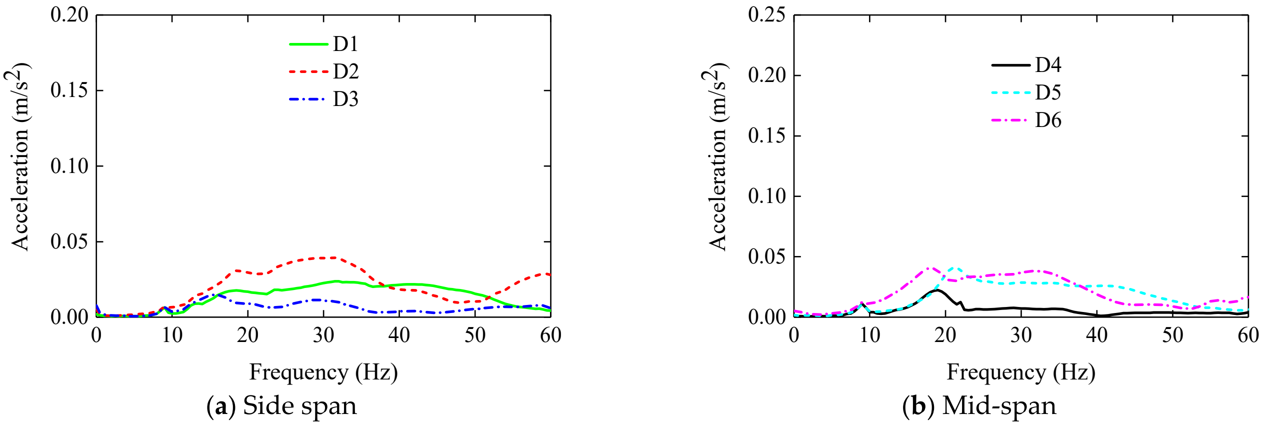

Figure 15. Frequency and acceleration curve of case S8.

Table 9. The FF of cases S7 and S8 (Hz).

Cases	Specimen	Constraint Forms	1	2	3	4	5	6
S7	C	4SC	15.0	15.0	14.0	14.5	14.5	14.5
S8	D	4SC	9.0	9.0	8.8	9.0	9.0	9.0

3.5. Different Structure Forms

Cases S4 and S8 are selected to compare and analyze the influence of different structural forms on the NVC of the roof system. The material of the S4 roof panel is AZA, and the width and occlusion form are 420 mm and 360°, respectively. The material of the S8 roof panel is AMM, and the width and occlusion form are 400 mm and 270°, respectively. The variation of PA and FF of cases S4 and S8 are drawn in Figure 16. The PA of case S8 is significantly greater than that of case S4, and the maximum difference is 83.7%. The maximum acceleration under cases S4 and S8 appear in the side span. Along the roof panel's length direction, each sensor's acceleration, in the case of S8, fluctuates wildly. The FF of case S8 is the same, about 9 Hz, and the FF of case S4 is about 15 Hz. The FF of case S4 is greater than that of case S8, and the difference between the two is about 60%.

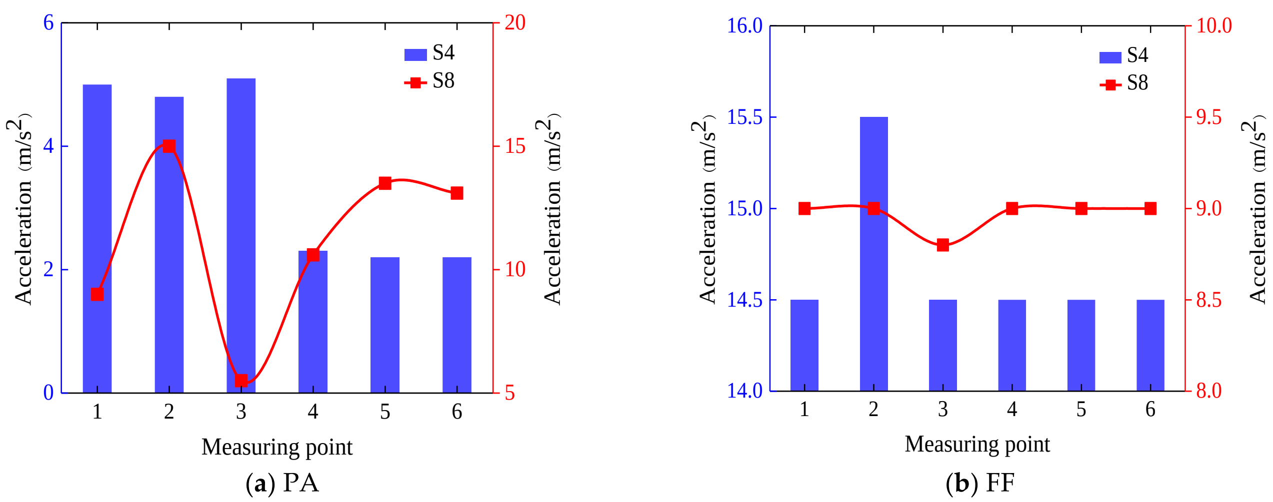

Figure 16. NVC of cases S4 and S8.

4. Conclusions

In this paper, the experimental investigation of the NVC of two kinds of typical structural form metal roof systems is carried out. The natural vibration frequency and PA of the roof panel at different spans of the side and middle span are analyzed, and the influence of different parameters on the natural frequency of the roof panel is further considered. The following conclusions can be drawn.

1. The test results of this paper have a certain reliability. The PA of the side span in case S1 is generally more significant than that of the middle span. The PA increases roughly along the length of the roof panel, with a maximum increase of 31.2%.
2. With the change of the boundary conditions, the influence on the acceleration of the side span of specimens A and C is greater than that of the middle span. Specimens A and C's maximum influence is 47.4% and 43.5%, respectively. The maximum influence of the boundary conditions on the first-order natural frequencies of specimens A and C is 7.4% and 20%, respectively.
3. The maximum influence of specimen width on specimens A and B's PA and the first natural frequency is 51.1% and 6.9%, respectively. The maximum influence of roof width on the PA and the FF of specimens C and D is 54.2% and 40%, respectively.
4. Under different structural forms, the PA of cases S4 and S8 appear in the side span. The FF of cases S4 and S8 are 9 Hz and 15 Hz, respectively. The maximum influence of the structural form on the PA and the FF of the roof systems is 83.7% and 60%, respectively.

It is worth noting that this paper only considers the dynamic characteristics of the roof system in the elastic stage, and does not consider the influence of external environmental loads and various influencing parameters on the mechanical properties and component damage of the roof system. After taking into account various factors related to the technical issue at hand, such as the geometry and mechanical properties of the panels, their boundary conditions, dissipation energy mechanism, and type of connections to the steel profiles below, it becomes evident that the dynamic behavior of the structure can be affected [30,31]. This, in turn, makes it challenging to evaluate natural frequencies and acceleration peaks. However, a possible solution to this dilemma would be to develop a comprehensive analytical or numerical model and incorporate deep learning and artificial intelligence techniques [32–34]. In the next step, the authors will use deep learning and artificial intelligence (DL & AI) methods [35–37] to carry out experimental and theoretical analysis of the mechanical properties and dynamic characteristics of the roof system under external environmental loads.

Author Contributions: Writing—original draft preparation, Z.X.; funding acquisition, Y.Z.; supervision, Y.Z. All authors have read and agreed to the published version of the manuscript.

Funding: National Natural Science Foundation of China (51778162), Y.Z.

Data Availability Statement: Data is contained within the article.

Conflicts of Interest: Author Z.X. has received research grants from Company Hunan Industrial Equipment Installation Co., Ltd. The remaining authors declare that the research was conducted in the absence of any commercial or financial relationships that could be construed as a potential conflict of interest.

References

1. Azzi, Z.; Habte, F.; Vutukuru, K.S.; Chowdhury, A.G.; Moravej, M. Effects of roof geometric details on aerodynamic performance of standing seam metal roofs. *Eng. Struct.* **2020**, *225*, 111303. [CrossRef]
2. Seek, M.W.; Avci, O.; McLaughlin, D. Effective standoff in standing seam roof systems. *J. Constr. Steel Res.* **2021**, *180*, 106590. [CrossRef]
3. Ou, T.; Wang, D.; Xin, Z.; Tan, J.; Wu, C.; Guo, Q.; Zhang, Y. Full-scale tests on the mechanical Behavior of a continuously welded stainless steel roof under wind excitation. *Thin-Walled Struct.* **2020**, *150*, 106680. [CrossRef]

4. Wu, T.; Sun, Y.; Cao, Z.; Yu, Z.; Wu, Y. Study on the wind uplift failure mechanism of standing seam roof system for performance-based design. *Eng. Struct.* **2020**, *225*, 111264. [CrossRef]
5. Lee, S.-H.; Lee, K.-K.; Woo, S.-S.; Cho, S.-H. Global vertical mode vibrations due to human group rhythmic movement in a 39 story building structure. *Eng. Struct.* **2013**, *57*, 296–305. [CrossRef]
6. Sivapathasundaram, M.; Mahendran, M. Development of fragility curves for localised pull-through failures of thin steel roof battens. *Eng. Struct.* **2016**, *124*, 64–84. [CrossRef]
7. Sivapathasundaram, M.; Mahendran, M. Numerical studies and design of thin steel roof battens subject to pull-through failures. *Eng. Struct.* **2017**, *146*, 54–74. [CrossRef]
8. Morrison, M.J.; Kopp, G.A. Analysis of wind-induced clip loads on standing seam metal roofs. *J. Struct. Eng.* **2010**, *136*, 334–337. [CrossRef]
9. Kumar, K.S. Prediction of wind-induced fatigue on claddings of low buildings. *Comput. Struct.* **2000**, *75*, 31–44. [CrossRef]
10. Myuran, K.; Mahendran, M. New test and design methods for steel roof battens subject to fatigue pull-through failures. *Thin-Walled Struct.* **2017**, *119*, 558–571. [CrossRef]
11. Myuran, K.; Mahendran, M. Unified static-fatigue pull-through capacity equations for cold-formed steel roof battens. *J. Constr. Steel Res.* **2017**, *139*, 135–148. [CrossRef]
12. Schroter, R.C. Air pressure testing of sheet metal roofing. *NRCA Second. Int. J. Roof. Technol.* **1985**, 254–260.
13. Ali, H.M.; Senseny, P.E. Models for standing seam roofs. *J. Wind. Eng. Ind. Aerodyn.* **2003**, *91*, 1689–1702. [CrossRef]
14. Li, H. Research on wind vibration performance of continuous welded stainless steel roof system. *Guangzhou Univ.* 2020. [CrossRef]
15. Domagalski, Ł. Comparison of the natural vibration frequencies of timoshenko and bernoulli periodic beams. *Materials* **2021**, *14*, 7628. [CrossRef] [PubMed]
16. Ji, W.; Luo, K.; Ma, W. Natural vibration frequency analysis for a PC continuous box-girder bridge with corrugated steel web based on the dynamic stiffness matrix. *J. Highw. Transp. Res. Dev.* **2020**, *14*, 65–74. [CrossRef]
17. Qikai, S.; Nan, Z.; Xiao, L. A dynamic stiffness matrix method for free vibrations of partial-interaction composite beams based on the Timoshenko beam theory. *J. Sound Vib.* **2022**, *520*, 116579.
18. Jiang, L.; Lai, Z.; Zhou, W. Improved finite beam element method for analyzing the flexural natural vibration of thin-walled box girders. *Adv. Mech. Eng.* **2017**, *9*, 1687814017726292. [CrossRef]
19. Zhang, Y.; Jiang, L.; Zhou, W.; Feng, Y. Shear lag effect and accordion effect on dynamic characteristics of composite box girder bridge with corrugated steel webs. *Appl. Sci.* **2020**, *10*, 4346. [CrossRef]
20. Jiang, L.; Yu, J.; Zhou, W.; Feng, Y.; Chai, X. Analysis of flexural natural vibrations of thin-walled box beams using higher order beam theory. *Struct. Des. Tall Spec. Build.* **2019**, *28*, e1659. [CrossRef]
21. Shen, J.; Pagani, A.; Arruda, M.R.T.; Carrera, E. Exact component-wise solutions for 3D free vibration and stress analysis of hybrid steel–concrete composite beams. *Thin-Walled Struct.* **2022**, *174*, 109094. [CrossRef]
22. Liu, Y.; Shang, F.; Xu, Z.; Wen, B. Study on natural characteristics of fiber metal laminates thin plates under cantilever boundary. *J. Vibroengineering* **2020**, *22*, 909–922. [CrossRef]
23. Van Do, T.; Hong Doan, D.; Chi Tho, N.; Dinh Duc, N. Thermal buckling analysis of cracked functionally graded plates. *Int. J. Struct. Stab. Dyn.* **2022**, *22*, 2250089. [CrossRef]
24. Doan, D.H.; Zenkour, A.M.; Thom, D.V. Finite element modeling of free vibration of cracked nanoplates with flexoelectric effects. *Eur. Physcial J. Plus* **2022**, *137*, 447. [CrossRef]
25. Dat, P.T.; Thom, D.V.; Luat, D.T. Free vibration of functionally graded sandwich plates with stiffeners based on the third-order shear deformation theory. *Vietnam. J. Mech.* **2016**, *38*, 103–122. [CrossRef]
26. Do, V.T.; Pham, V.V.; Nguyen, H.N. On the development of refined plate theory for static bending behavior of functionally graded plates. *Math. Probl. Eng.* **2020**, *2020*, 2836763. [CrossRef]
27. Nguyen, H.N.; Hong, T.T.; Vinh, P.V.; Thom, D.V. An Efficient Beam Element Based on Quasi-3D Theory for Static Bending Analysis of Functionally Graded Beams. *Materials* **2019**, *12*, 2198. [CrossRef] [PubMed]
28. El-Kafafy, M.; Peeters, B.; Guillaume, P.; De Troyer, T. Constrained maximum likelihood modal parameter identification applied to structural dynamics. *Mech. Syst. Signal Process* **2016**, *72–73*, 567–589. [CrossRef]
29. El-Kafafy, M.; De Troyer, T.; Guillaume, P. Fast maximum likelihood identification of modal parameters with uncertainty intervals: A modal model-based formulation. *Mech. Syst. Signal Process* **2013**, *37*, 422–439. [CrossRef]
30. Jia, Z.; Wang, W.; Zhang, J.; Li, H. Contact high-temperature strain automatic calibration and precision compensation research. *J. Artif. Intell. Technol.* **2022**, *2*, 69–76.
31. Khan, A.; Shin, J.K.; Lim, W.C.; Kim, N.Y.; Kim, H.S. A deep learning framework for vibration-based assessment of delamination in smart composite laminates. *Sensors* **2020**, *20*, 2335. [CrossRef] [PubMed]
32. Du, H.; Du, S.; Li, W. Probabilistic time series forecasting with deep non-linear state space models. *CAAI Trans. Intell. Technol.* **2023**, *8*, 3–13. [CrossRef]
33. Hu, X.; Kuang, Q.; Cai, Q.; Xue, Y.; Zhou, W.; Li, Y. A coherent pattern mining algorithm based on all contiguous column bicluster. *J. Artif. Intell. Technol.* **2022**, *2*, 80–92.
34. Zhao, H.; Ma, L. Several rough set models in quotient space. *CAAI Trans. Intell. Technol.* **2022**, *7*, 69–80. [CrossRef]

35. Zhang, Z.; Luca, G.D.; Archambault, B.; Chavez, J.; Rice, B. Traffic dataset and dynamic routing algorithm in traffic simulation. *J. Artif. Intell. Technol.* **2022**, *2*, 111–122. [CrossRef]
36. Altabey, W.A. Applying deep learning and wavelet transform for predicting the vibration behavior in variable thickness skew composite plates with intermediate elastic support. *J. Vibroengineering* **2021**, *23*, 14. [CrossRef]
37. Hsiao, I.H.; Chung, C.Y. AI-infused semantic model to enrich and expand programming question generation. *J. Artif. Intell. Technol.* **2022**, *2*, 47–54. [CrossRef]